Vortex-induced nonlinearity and the effects of ion irradiation on the high-frequency response of NbTi films

Vortex-induced nonlinearity and the effects of ion irradiation on the high-frequency response of NbTi films

Gianluca Ghigo[a,b], Michela Fracasso[a,b], Roberto Gerbaldo[a,b], Daniele Torsello[a,b], Cristian Pira[c], Giovanni Marconato[c], Matteo Fretto[d], Natascia De Leo[d], Laura Gozzelino[a,b]

[a]*Department of Applied Science and Technology, Politecnico di Torino, c.so Duca degli Abruzzi 24, Torino, 10129, Italy*
[b]*Istituto Nazionale di Fisica Nucleare, Sez. Torino, via P. Giuria 1, Torino, 10129, Italy*
[c]*Istituto Nazionale di Fisica Nucleare, Laboratori Nazionali di Legnaro, viale dell'Università 2, Legnaro (PD), 35020, Italy*
[d]*Istituto Nazionale di Ricerca Metrologica, strada delle Cacce 91, Torino, 10135, Italy*

Abstract

The microwave response of superconducting devices can be affected by nonlinearity effects of both intrinsic and extrinsic origin. In this study, we report on the nonlinear behavior of NbTi microwave resonators, in the presence of dc magnetic fields up to 4 T. The aim of this work is to characterize the vortex-induced nonlinearity, which in these conditions of frequency (11 GHz) and fields is expected to give the major contribution to dissipation, when the circulating rf current exceeds a given threshold. Nonlinearity is investigated by analyzing Q-degradation and resonance curve distortion as a function of the input rf power, while the emergence of sharp discontinuities is associated to the existence of an rf limiting current density. The current densities corresponding to the onset of these features are compared to the critical current density from dc measurements, helping us to outline a comprehensive picture. Moreover, the pinning constant was extracted as a function of temperature by means of a Gittleman-Rosenblum analysis, revealing the prominent role of δT_c-type pinning. We also analyzed the effects of introducing controlled artificial disorder and pinning sites through 1.5−MeV proton irradiation. After irradiation, we observed an increase of both the pinning constant and the in-field nonlinearity threshold and limiting current.

Keywords: NbTi films, microwave superconductivity, proton irradiation, nonlinear vortex dynamics, vortex pinning, microwave coplanar resonators

1. Introduction

The employment of superconducting coatings in technological applications, as for example rf cavities in particle accelerators [1], or − more recently − in axion haloscopes [2], suffers from the limits imposed by the onset of nonlinear response. Although this issue is known since the '70s for Nb SRF cavities [3], the literature is lacking data about nonlinear effects in NbTi films in the high frequency range, and virtually nothing is known about nonlinearity in this material in conditions of high dc magnetic field, i.e. when the vortices are expected to give the major contribution to dissipation and nonlinearity.

In this work, we analyze the nonlinear response of microwave coplanar waveguide resonators (CPWRs) made by patterning NbTi films. Nonlinearity is characterized through the study of the degradation of the quality factor of the resonator, at increasing values of the circulating rf currents. We define the rf current density value corresponding to the onset of nonlinearity, j_{nl}^{rf}, and the limiting rf current density, above which the resonator or part of it switches to the normal state, j_{lim}^{rf}. Then, to highlight the high-frequency peculiar aspects, we compare these current densities to the onset of dissipation obtained by dc current-voltage characteristics, j_{th}^{dc}. By the comparison, we discuss the mechanisms of nonlinearity and dissipation induced by the vortex dynamics and the role of pinning. The specific pinning mechanism in the samples is investigated through the temperature dependence of the pinning constant, obtained by a Gittleman-Rosenblum analysis. Finally, we modify the pinning landscape by 1.5-MeV proton irradiation and further investigate the interaction of vortices with pinning centers at high frequency.

2. Materials and methods

2.1. NbTi deposition and CPWR fabrication

$Nb_{31}Ti_{69}$ films were deposited onto quartz substrates by dc magnetron sputtering. All details were given in a recent work [4]. In brief, in the deposition system a target-sample distance of 11 cm was set and the chamber was baked at 600 °C before starting the deposition. The growth process was carried out at 550 °C using Ar as working gas, with a pressure of $6{\cdot}10^{-3}$ mbar.

Patterning is challenging, due to the quite high thickness of the films usually required as coating for haloscopes (1-3 μm) and to the need of sharp, well defined, and clean edges, since in CPWRs most of the rf currents flow at the edges. Therefore, devices were produced through a combination of laser optical lithography, sputtering deposition of an Al hard mask (120 nm thick), and highly directional Reactive Ion Etching (SF_6 at $2 \cdot 10^{-2}$ mbar). Further details were given in Ref. 4.

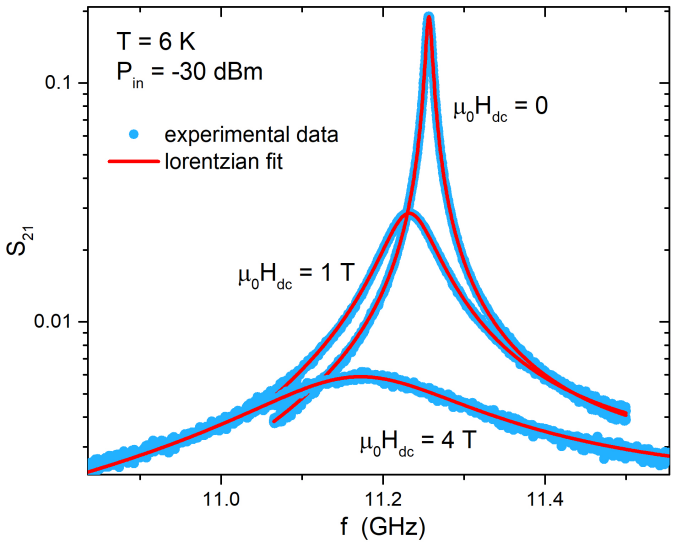

Figure 1: Resonance curves for different values of dc magnetic field, from 0 to 4 T, in the low rf-power linear regime. Experimental data are fitted by the function reported in Eq.1.

2.2. Measurements and irradiation

The complex transmission coefficient of the CPWRs, S_{21} (ratio of the voltage transmitted to the incident voltage), was measured as a function of the driving frequency, f, by means of a vector network analyzer (VNA) near the resonance frequency of the device. Resonance curves were obtained in different conditions of temperature, dc magnetic field (applied perpendicular to the film plane), and rf input power (examples are given in Fig.1).

Dc measurements, resistivity as a function of temperature and current−voltage characteristics, were performed with 15 and 96-μm-wide Hall bars, by a standard four probes technique. In order to minimize the thermoelectric voltage offset and time drift, a pulse-delta mode was employed [5], by inverting the bias current polarity and by averaging over some voltage measurements.

Both CPWRs and Hall bars were irradiated in vacuum at room temperature with a 1.5 MeV proton beam at the AN2000 facility of the INFN - Laboratori Nazionali di Legnaro, Italy, up to a fluence of 4×10^{16} cm^{-2}. Protons were directed perpendicular to the film plane and implanted into the quartz substrate, at a depth of 27 μm, as calculated by means of the Monte Carlo SRIM code [6]. The same code can be used to evaluate the displacements per atom (dpa), discriminating the values for Nb and Ti atoms. Starting from displacement energies of 78 eV and 30 eV for Nb and Ti, respectively [7], it turns out that in our experiment dpa(Nb)$\approx 1.4 \cdot 10^{-3}$ and dpa(Ti)$\approx 2.2 \cdot 10^{-3}$.

3. Results and discussion

3.1. Microwave linear regime

A first set of CPWR measurements was done within the linear regime, i.e. with low input rf power ($-30 \div -20$ dBm). In Fig.1, resonance curves (magnitude of S_{21} as a function of frequency) measured at $T = 6$ K in different dc magnetic fields are reported. All these curves can be fitted well by the function

$$|S_{21}(f)| = \frac{\hat{S}_{21}}{\sqrt{1 + Q_L^2 \left(\frac{f}{f_0} - \frac{f_0}{f}\right)^2}} \quad (1)$$

where f_0 is the resonance frequency, $\hat{S}_{21}$ is the maximum $|S_{21}|$ value at the resonance, Q_L is the loaded quality factor (the unloaded quality factor, Q_0, is obtained by accounting for the coupling coefficients [8]). The good quality of the fit assures that even in the presence of vortices (at high dc fields), for these values of the rf input power the linearity regime is preserved: the addition of a dc magnetic field increases dissipation but does not drive the system to a nonlinear regime. Linear measurements in zero dc field as a function of temperature were used to determine the London penetration depth and the surface resistance, as discussed in details in Refs.9, 8, 4. For our NbTi films, it turns out that the penetration depth extrapolated to zero temperature is $\lambda_L(0) \approx 300$ nm, [4] an estimation consistent with literature for similar compositions [10, 11].

3.2. Nonlinear effects

The relatively low power-handling capability of CPWRs turns out to be an advantage when nonlinear effects have to be studied. In fact, even with the moderate rf power available in standard VNAs, the device can be driven to nonlinear regimes. Figure 2 shows how nonlinearity emerges as the input power is increased. The curve obtained with $P_{in} = -20$ dBm is in the linear regime and can be fitted well by Eq.1. For increasing input power, the curves start to distort gradually, with decreasing values of both f_0 and $\hat{S}_{21}$ (e.g. curves at -2, $+2$, and $+3.4$ dBm). This behavior has been observed in other superconductors [12, 13], and this issue for Nb rf cavities has been known since the '70s [3]. Although it is generally attributed to global heating effects, the asymmetry of the curves − due to the power dependence of the surface reactance − may have different either intrinsic or extrinsic origins: pair breaking, nucleation of high-frequency vortices, Abrikosov vortex dynamics, granularity, or other effects. Thus, the mechanisms producing such nonlinearity must be discussed case by case.

When P_{in} is further increased, another nonlinear effect emerges, in the form of abrupt jumps in the resonance curve that temporary drive the response to another curve, then recovering the original one (e.g., for the curves at $P_{in} \geq 3.5$ dBm). This behavior can be ascribed to fast switching of the sample or a part of it (i.e. a weak link) to the normal state, with the consequent nucleation of a localized hot-spot, that vanishes as the superconducting state is recovered, when the rf current flowing in the resonator decreases [14]. This happens when the density of the rf currents approaches a critical value [15], but, again, what the origin of this critical value is (whether depairing, depinning, etc.) has to be investigated case by case.

In order to characterize the onset of nonlinearity, we plot in Fig.3 the normalized resonance parameters as a function of the

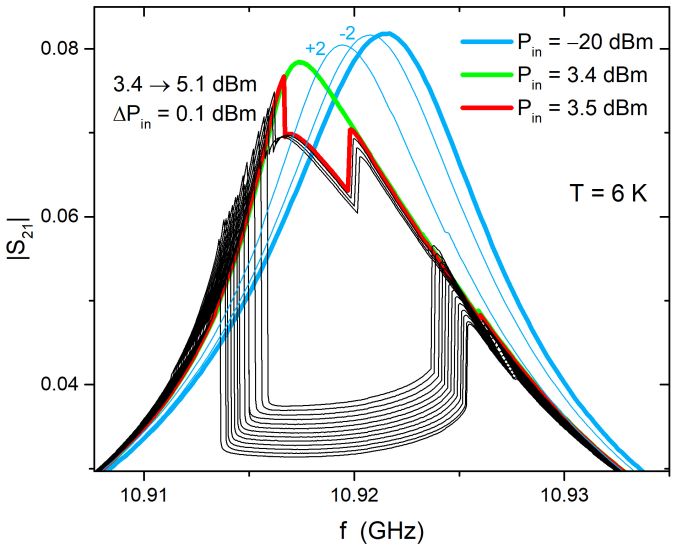

Figure 2: CPWR resonance curves measured for different values of input rf power, P_{in}, from the linear regime to the nonlinear one. Reference curves are highlighted, corresponding to: −20 dBm input power (linear regime); +3.4 dBm and +3.5 dBm, just before and after the first weak link switching.

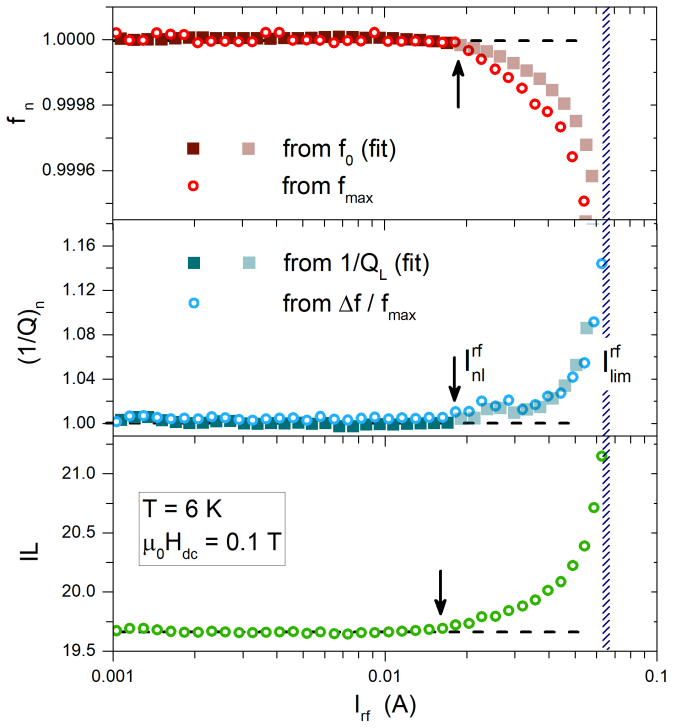

Figure 3: Resonance frequency, normalized by its low-power value (a), inverse of the loaded quality factor, normalized by its low-power value (b), and insertion loss (c) as a function of the rf current circulating in the CPWR at the resonance, calculated by Eq.2. Data were extracted from Lorentzian fits of the resonance curves (f_0, Q_L) and directly from the experimental $S_{21}(T)$ resonance curves (frequency at the maximum, f_{max}, curve width at −3 dB, Δf), insertion loss $IL = -20\text{Log}(|S_{21}|^{max})$). The limiting rf current I_{lim}^{rf} is the maximum current flowing in the CPWR.

rf current circulating in the resonator at the resonance, I_{rf}. This current can be calculated in CPWRs as [16]

$$I_{rf} = \sqrt{\frac{4\hat{S}_{21} Q_L P_{in}}{\pi Z_0}} \tag{2}$$

where $Z_0 \approx 50\ \Omega$ is the characteristic impedance of the line. In the linear regime – low I_{rf} values – the parameters do not show a dependence on the circulating current, while at higher values a clear I_{rf} dependence emerges, indicating nonlinearity. Of course, in the nonlinear regime the fitting parameters f_0 and Q_L start to lose their significance, since the resonance deviates from the Lorentzian shape. Therefore we also plot the frequency of the $|S_{21}(f)|$ maximum in the upper panel, and $\Delta f/f$ in the medium panel, where Δf is the resonance curve width at −3 dBm, as an estimation of $1/Q_L$. It is clear from the figure that, in any case, the threshold between the linear and the nonlinear regimes can be well determined as the rf current I_{nl}^{rf} indicated by the arrows. Small differences between these thresholds for f_0, $1/Q_L$, and the insertion loss ($IL = -20\text{Log}(|S_{21}|^{max})$) are probably due to small differences in inductive, resistive and dissipation nonlinearity [17].

It is also clear that there is an upper limit in the rf current that can flow in the device. This limiting value is here labeled I_{lim}^{rf} and corresponds to the onset of switching, when present, or simply as a vertical asymptote, as in Fig.3.

Figure 4 shows the resonance frequency and the quality factor, both normalized to their values at low input power, as a function of the rf circulating current for different values of applied dc field, up to 4 T. Up to 0.3 T of dc field, the sudden jump characterizing the limiting rf current was directly observed and I_{lim}^{rf} was calculated by means of Eq.2 with $Q_L = f/\Delta f$. These values are reported in panel (b) as star symbols. The I_{lim}^{rf} values for the other dc fields were deduced from the shift of the curves at the level of the black dashed line in panel (b). In any case, I_{lim}^{rf} is actually a limiting current, since the current flowing in the device cannot be further increased even upon supplementary input power. However, the mechanisms responsible of the existence of a limit could be different in the two cases, connected to an intrinsic limit when the discontinuity appears, and more related to the vortex dynamics when the limit is reached smoothly. This will be further discussed in Section 3.6, where the results of the addition of pinning by proton irradiation will be shown.

In order to translate these reference currents in current density values, one should consider that I_{rf} is distributed in the CPWR in a non-homogeneous way, with maxima at the edges. The edge region extends over the edge penetration depth $\lambda_\perp$, which is related to the London penetration depth by $\lambda_\perp = \lambda_L \coth[d/(2\lambda_L)]$, where d is the film thickness. In this edge region [18]:

$$j_{rf} = j_{rf}^{max} = \frac{I_{rf}}{K\left(\frac{w}{d}\right) d \sqrt{w\lambda_\perp \left[1 - \left(\frac{w}{d}\right)^2\right]}} \tag{3}$$

where $K(x)$ is the complete elliptic integral of the first kind and w is the width of the CPWR stripline. Eq.3 allows computing the maximum value of current density in the CPWR when the total current I_{rf} is circulating (the dependence of the pen-

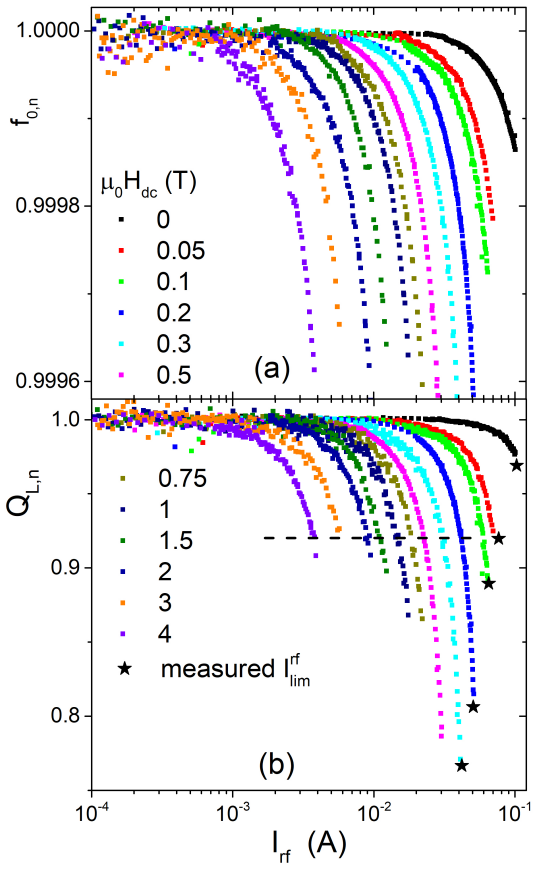

Figure 4: (a) Resonance frequency normalized by its low-power value, as a function of the rf current circulating in the CPWR at the resonance, for different values of applied dc magnetic field. (b) Normalized unloaded quality factor. Star symbols indicate limiting rf current values, obtained as the maximum current just before jump occurrence in the resonance curves. The black dashed line was used to determine the shifts in I^{rf}_{lim} as a function of dc field, when jumps were not observed.

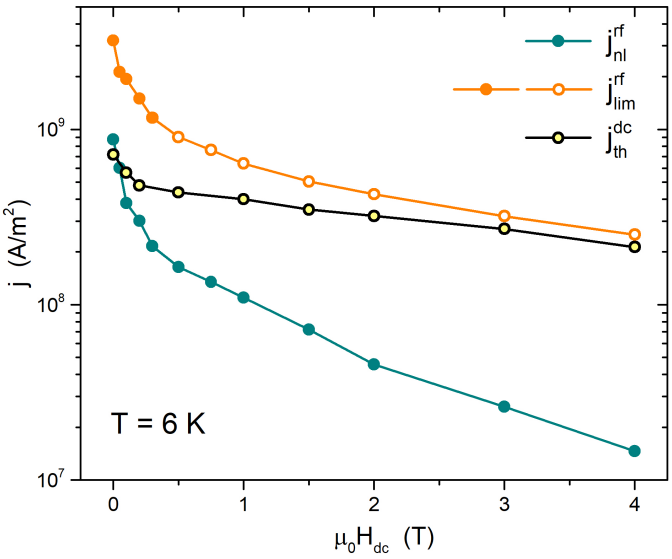

Figure 5: Comparison among the reference current densities discussed throughout the text: j^{rf}_{nl} is the threshold current density above which nonlinearities emerge; j^{rf}_{lim} is the limiting rf current density (solid symbols: data measured in the presence of a jump, open symbols: extrapolated data, see main text); j^{dc}_{th} indicates the onset of dissipation in current-voltage dc characteristics.

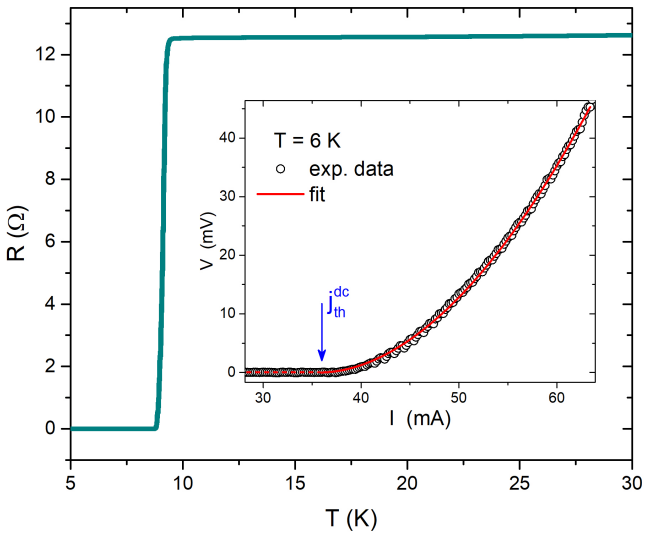

Figure 6: Dc resistance vs. temperature curve of a NbTi Hall bar, at zero field. In the inset, a current-voltage curve is reported at the temperature of 6 K and for an applied dc magnetic field of 1 T. The fit to a flux creep model is shown (see text for details) and the onset of dissipation j^{dc}_{th} is indicated by an arrow.

etration depth on the dc field was taken into account). We assume that the reference currents I^{rf}_{nl} and I^{rf}_{lim} are connected to the maximum value of the flowing current density. Thus, one can obtain from Eq.3 the nonlinearity threshold current density $j^{rf}_{nl}(H_{dc})$ and the limiting current density $j^{rf}_{lim}(H_{dc})$, that are shown in Fig.5 at $T = 6$ K, and compared to dc measurements, described and discussed below.

3.3. Dc measurements

Figure 6 shows the dc resistance vs. temperature curve for a NbTi Hall bar, with the superconducting transition occurring at about 9 K. In the inset, we provide an example of current-voltage (I-V) curve measured at $T = 6$ K and in a dc field of 1T, applied perpendicular to the film plane. The experimental I-V curves are well reproduced by fitting the data with the electric field-current density (E-j) relationship predicted by the percolation model described in Ref.19. In the framework of this model, no power dissipation is expected below a certain current density threshold, j^{dc}_{th}, where the vortices are 'frozen' in the superconductor [20]. Above this threshold, the superconductor enters the 'flux creep' regime where the vortices start to have enough energy to hop from one pinning center to another one, percolating across the sample and generating dissipation. Note that the j^{dc}_{th} threshold is lower than the depinning critical current density, defined as the value at which the Lorentz force equals the pinning force, thus removing the pinning potential barrier, and above which the virtually free 'flux flow' regime sets up. The j^{dc}_{th} values yielded by fitting the I-V curves measured at different applied fields are plotted in Fig.5.

3.4. Reference current densities

We now turn to comparing the current densities defined above, with the aim of discussing the differences induced by the frequency regime. It was suggested that the nonlinear microwave behavior is strongly related to the dc critical current density of the superconductor, as reported for YBCO [21] and for MgB_2 [8]. For other superconductors (such as Nb alloys) this relation is more questionable [22]. We found a complex picture, summarized in Fig.5, that we can tentatively describe as follows.

The onset of nonlinearity j_{nl}^{rf} in zero field matches quite well the onset of dissipation in dc measurements, j_{th}^{dc}. However, when a dc field is applied the two current densities behave differently, with a much steeper drop for j_{nl}^{rf}. This behavior can be explained by the fact that in dc conditions dissipation emerges when vortices start to escape from the pinning centers (creep), while in rf measurements vortices oscillate even when they are confined in the pinning potential well, where they can experience a flux flow resistivity. Therefore, the sharp degradation of j_{nl}^{rf} can be attributed to the fact that the confined vortices can probe a non parabolic potential at the bottom of the well.

It is straightforward to associate j_{lim}^{rf} to an rf critical current density, that at zero-field is higher than j_{th}^{dc}. It may be worth recalling here that j_{th}^{dc} is not the dc critical current density (which is somehow higher), but the minimum current density allowing the vortices to escape from a pinning center [19], being the materials still in the superconducting state. However, the rf critical current density could be reasonably higher than the dc counterpart, due to the virtual absence of relaxation in microwave measurements. Notwithstanding, j_{lim}^{rf} shows an initial steep field decrease, due to the flux-flow resistance term mentioned above.

Remarkably, at high dc fields j_{lim}^{rf} matches j_{th}^{dc} very well. This result is not trivial, since the two reference current densities rely on different and in principle independent properties of the pinning potential well, i.e. on its shape for the former rf current and on its height for the latter dc one. This could be explained by the increasing importance of the intervortex interaction at higher applied field [23], where it dominates over the details of single potential wells, and the qualitative differences between dc and rf dynamics start to decrease and eventually to vanish.

3.5. Flux pinning mechanism

We used the Gittleman-Rosenblum model [24] to calculate the pinning constant k_p as a function of temperature, from our CPWR measurements. Details were given in a previous recent paper [4], where the $k_p(H_{dc})$ dependence was reported, pointing to the presence of a collective pinning regime. Figure 7 shows the k_p temperature dependence at $\mu_0 H_{dc} = 1$ T (with k_p spanning over three decades), that is used here to investigate the specific pinning mechanism. Within the collective pinning regime, k_p is generally determined by the vortex interaction with the pinning sites and by the vortex elasticity, according to the expression [25, 26] $k_p = U_c/(\xi^2 L_c) = \mu_0 H_c^2 \delta^{2/3}$, where U_c is the pinning potential, L_c is the collective pinning length, H_c is the thermodynamic critical field, $H_c = \sqrt{H_{c1} H_{c2}}$, and δ is a dimensionless parameter, depending on temperature and pinning type [26]. Thus, $k_p(t) \sim H_{c1}(t) H_{c2}(t) \delta(t)^{2/3}$, where $t = T/T_c$ is the reduced temperature. Different temperature dependencies are expected for pinning induced by local fluctuations of critical temperature (δT_c disorder) or mean free path ($\delta\ell$ disorder), namely $\delta \sim (1-t)^{-1/2}$ in the former case and $\delta \sim (1-t)^{3/2}$ in the latter one. As for the critical fields, $H_{c1}(t) \sim \lambda_L(t)^{-2} \sim (1-t^4)$ (the functional form for λ_L was validated by our CPWR data, see Ref.4), and for $H_{c2}(t)$ we fitted our data [4] with the phenomenological function $H_{c2} = H_{c2,0}(1-t^\beta)$, so finally we get

$$k_p(t) \sim (1-t^4)(1-t^\beta)(1-t) \qquad (\delta\ell \textit{ pinning}) \tag{4}$$

$$k_p(t) \sim (1-t^4)(1-t^\beta)(1-t)^{-1/3} \ (\delta T_c \textit{ pinning}) \tag{5}$$

Figure 7 clearly shows that, in the studied temperature range, experimental data are much better described by the δT_c pinning curve (Eq.5) than by the $\delta\ell$ one (here, the $\beta = 4.1$ value was used, determined for the specific CPWR, see discussion in Ref.4). Slight discrepancy of data from the δT_c curve could originate from a small contribution of $\delta\ell$ pinning. It is also possible that $\delta\ell$-type pinning becomes more important at lower temperatures. The consistency of our data with the δT_c mechanism for pinning is reasonable for at least two reasons: (i) due to granularity and to the presence of proximized $\alpha-$Ti inclusions, we expect that the Ti distribution is not uniform in the material, and it is well known that T_c in NbTi critically depends on the local Ti content. (ii) We observed an anomaly in the resonance frequency near T_c (the dip shown in the inset of Fig.7) that has recently been observed also in Nb SRF cavities [27], and that was explained [28] by a spread in T_c values.

Concerning granularity, the presence of a granular structure with well-connected sub-micrometric grains was observed in our films by FESEM (field emission scanning electron microscopy) and can also be inferred from the dc resistivity superconducting to normal state transition, with moderately large width of 0.4-0.5 K, as already reported in Ref.4. Generally, granularity can be invoked to explain several properties of our films beyond δT_c pinning, e.g. the peculiar $H_{c2}(T)$ dependence [4], and the difference between the low-field dc and rf critical current densities.

3.6. Effects of proton irradiation

Proton irradiation is expected to modify the δT_c-pinning scenario first of all through the introduction of further disorder in the Ti distribution in the material. Note that Nb and Ti have different cross sections for protons at MeV energies [29] and we actually calculated different dpa values for the two atomic species that in our specific case differ by 60% (see Section 2.2). Moreover, defects themselves could locally influence T_c with a mechanism already reported for pure Nb. In fact, in the presence of gap anisotropy, even non-magnetic impurity scattering is pair breaking, leading to the violation of Anderson's theorem and a suppression of T_c [30, 31].

Figures 8 and 9 illustrate the efficiency of proton irradiation in improving both the pinning capability and the linearity range. In Fig.8, we report the current density percentage variation of the irradiated CPWR with respect to the very same

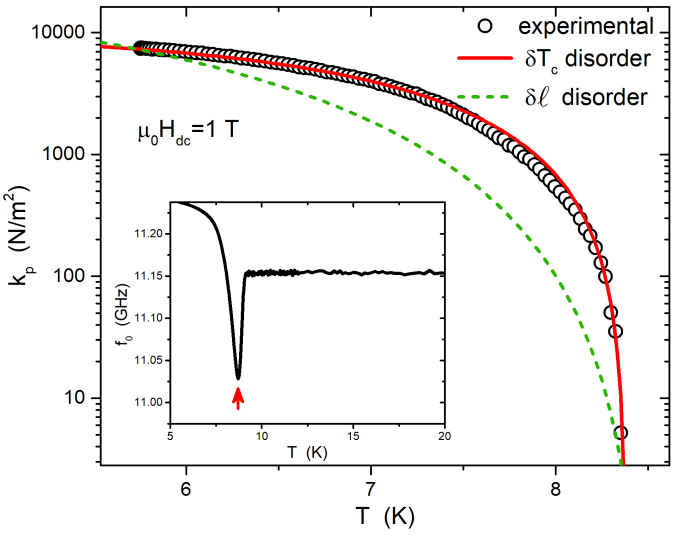

Figure 7: Pinning constant k_p as a function of temperature, for an applied dc field of 1 T. The red line is the behavior expected for δT_c pinning, according to Eq.5, while the green dashed line shows what would be the temperature dependence in the case of $\delta\ell$ pinning. In the inset, the observed $f_0(T)$ anomaly is reported.

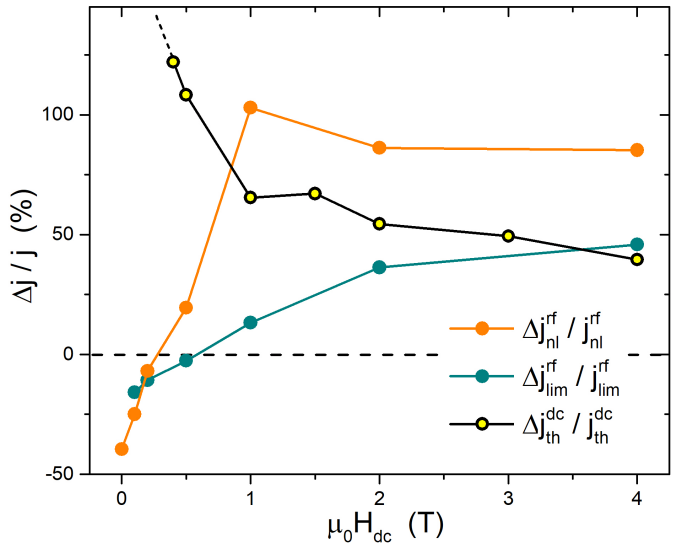

Figure 8: Effects of proton irradiation on the reference current densities, at T = 6 K, as a function of dc applied field: percentage variation of the nonlinearity threshold current density j_{nl}^{rf}, of the limiting current density j_{lim}^{rf}, and of the dc current density at the onset of dissipation, j_{th}^{dc}. The same CPWR and Hall bar were measured before and after irradiation. The dotted line at the dc curve indicates that at low field the increment is undefined but surely higher than 100 % (we measured the current density before irradiation, but after irradiation we could not because the critical current was higher than 100 mA, which is the limit of our apparatus).

device before irradiation. It turns out that, after an initial decrease at low fields, both j_{nl}^{rf} and j_{lim}^{rf} start to increase above about $\mu_0 H_{dc}$ = 0.25 T and 0.5 T, respectively. These curves, overall increasing with field, show an opposite trend with respect to the dc current density, showing a high increment at low fields, decreasing with field. This opposite behaviour could be justified considering that in the dc regime at low field the creep

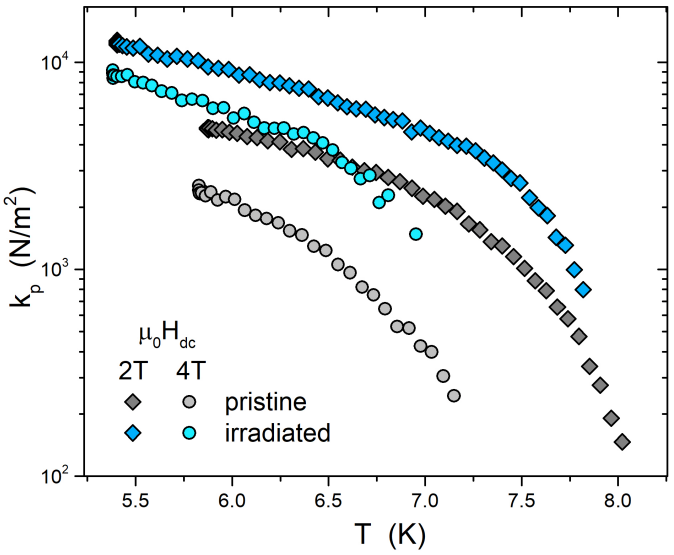

Figure 9: Pinning constant as a function of temperature for different applied magnetic fields, for the same CPWR before and after proton irradiation.

phenomenon is dominated by hopping of single vortices from one pinning center to another one. In such a scenario, the addition of new point-like defects can help to contrast the vortex movement more effectively than in the medium-high field region, where the intervortex interaction also play a relevant role.

The pinning constant as a function of temperature (at $\mu_0 H_{dc}$ = 2 T and 4 T) is shown in Fig.9, where the improvement given by proton irradiation clearly emerges.

4. Conclusions

The main aim of this study was to characterize the nonlinear behavior of NbTi in high frequency and high magnetic field conditions, and to discuss its origin, in particular to distinguish the conditions at which the vortex-motion contribution is predominant. Accordingly, we developed a measurement and analysis protocol to define reference current density values and pinning parameters. Among the results, we obtained the determination of the linearity and nonlinearity regions in the $j(H_{dc})$ diagram (Fig.5), the determination of the main flux pinning mechanism, of δT_c type (Fig.7), the determination of the pinning parameters (Fig.9) and their improvements upon 1.5-MeV proton irradiation (Figs.8 and 9).

In fact, the introduction of new pinning centers by proton irradiation allowed us to elaborate about the origin of nonlinearity. We argue that the limiting rf current (which can be read as the microwave critical current density) and the threshold of nonlinearity can be enhanced by introducing further pinning centers by proton irradiation only in a field region where vortex-dynamics-induced dissipation and nonlinearity are dominant, since in this case they can be mitigated by an increased pinning efficiency. This is what happens above $\mu_0 H_{dc}$ = 0.25 T and 0.5 T for j_{nl}^{rf} and j_{lim}^{rf}, respectively. On the contrary, at low fields the increase of pinning is not as effective and the concurrent effect of the additional defects, i.e. the increase of charge

carrier scattering, affects the superfluid density and in turn the more fundamental and intrinsic mechanisms of dissipation and nonlinearity. This is a behavior specific of the high frequency regime, since the dc characterization showed an opposite trend, with a positive current shift after irradiation that decreases with field, therefore with the highest increase precisely at the lowest field values. The prevailing contribution of vortex motion only above a given field for the microwave response is suggested after all by the direct experimental observation. In particular, discontinuities in the response (see Fig.2) implying the presence of bistable states connected to sharp transitions (as expected for weak-link switching, phase slip, critical velocity, etc.) could only be achieved at low fields (star symbol in Fig.4 and hollow symbols in Fig.5), while smooth transitions connected with the evolution of a critical state where pinning is dominant occur at higher fields.

CRediT authorship contribution statement

Gianluca Ghigo: Conceptualization, Methodology, Investigation, Supervision, Writing - original draft. Michela Fracasso: Data curation, Writing - review & editing. Roberto Gerbaldo: Investigation, Data curation. Daniele Torsello: Formal analysis, Validation, Writing - review & editing. Cristian Pira: Resources, Validation, Writing - review & editing. Giovanni Marconato: Data curation. Matteo Fretto: Investigation, Resources. Natascia De Leo: Investigation, Writing - review & editing. Laura Gozzelino: Investigation, Supervision, Writing - review & editing.

Declaration of Competing Interest

The authors declare that they have no known competing financial interests or personal relationships that could have appeared to influence the work reported in this paper.

Data availability

The data that support the findings of this study are available from the corresponding author upon reasonable request.

Acknowledgements

This work was supported by INFN-CSN5 under the experiment SAMARA. D.T. acknowledges that his contribution was carried out within the Ministerial Decree no. 1062/2021 and received funding from the FSE REACT-EU - PON Ricerca e Innovazione 2014-2020. This manuscript reflects only the authors' views and opinions, neither the European Union nor the European Commission can be considered responsible for them.

References

[1] G. Ciovati, Superconducting radiofrequency cavities, in: Handbook of Superconductivity, CRC Press, 2023, pp. 583–594.

[2] D. Alesini, C. Braggio, G. Carugno, N. Crescini, D. D'Agostino, D. Di Gioacchino, R. Di Vora, P. Falferi, S. Gallo, U. Gambardella, C. Gatti, G. Iannone, G. Lamanna, C. Ligi, A. Lombardi, R. Mezzena, A. Ortolan, R. Pengo, N. Pompeo, A. Rettaroli, G. Ruoso, E. Silva, C. C. Speake, L. Taffarello, S. Tocci, Galactic axions search with a superconducting resonant cavity, Phys. Rev. D 99 (2019) 101101. doi:10.1103/PhysRevD.99.101101.

[3] J. Halbritter, Change of eigenstate in a superconducting RF cavity due to a nonlinear response, Journal of Applied Physics 41 (11) (1970) 4581–4588.

[4] G. Ghigo, D. Torsello, L. Gozzelino, M. Fracasso, M. Bartoli, C. Pira, D. Ford, G. Marconato, M. Fretto, I. De Carlo, et al., Vortex dynamics in nbti films at high frequency and high dc magnetic fields, Scientific Reports 13 (1) (2023) 9315.

[5] https://www.tek.com/en/documents/product-article/keithley-low-level-measurements-handbook—7th-edition.

[6] J. F. Ziegler, M. D. Ziegler, J. P. Biersack, Srim–the stopping and range of ions in matter (2010), Nuclear Instruments and Methods in Physics Research Section B: Beam Interactions with Materials and Atoms 268 (11-12) (2010) 1818–1823.

[7] A. Konobeyev, U. Fischer, Y. Korovin, S. Simakov, Evaluation of effective threshold displacement energies and other data required for the calculation of advanced atomic displacement cross-sections, Nuclear Energy and Technology 3 (3) (2017) 169–175. doi:https://doi.org/10.1016/j.nucet.2017.08.007.

[8] G. Ghigo, D. Torsello, Microwave Analysis of Unconventional Superconductors with Coplanar-Resonator Techniques, Springer, 2022.

[9] G. Ghigo, G. A. Ummarino, L. Gozzelino, T. Tamegai, Penetration depth of $Ba_{1-x}K_xFe_2As_2$ single crystals explained within a multiband eliashberg $s\pm$ approach, Phys. Rev. B 96 (2017) 014501. doi:10.1103/PhysRevB.96.014501.

[10] C. Benvenuti, M. Minestrini, M. Hauer, S. Calatroni, G. Orlandi, W. Weingarten, (NbTi)N and NbTi coatings for superconducting accelerating cavities (no. CERN – MT – DI – 91 – 5), Proc. Fifth Workshop RF Supercond. (1991) 518–526.

[11] Y. Bychkov, R. Herzog, I. Khukhareva, Thermal conductivity and electrical resistivity of NbTi alloys at low temperatures, Cryogenics 21 (12) (1981) 741–745. doi:https://doi.org/10.1016/0011-2275(81)90219-8.

[12] B. Abdo, E. Segev, O. Shtempluck, E. Buks, Nonlinear dynamics in the resonance line shape of NbN superconducting resonators, Phys. Rev. B 73 (2006) 134513. doi:10.1103/PhysRevB.73.134513.

[13] L. F. Cohen, A. L. Cowie, A. Purnell, N. A. Lindop, S. Thiess, J. C. Gallop, Thermally induced nonlinear behaviour of HTS films at high microwave power, Superconductor Science and Technology 15 (4) (2002) 559–565. doi:10.1088/0953-2048/15/4/313.

[14] G. Ghigo, R. Gerbaldo, L. Gozzelino, F. Laviano, G. Lopardo, E. Monticone, C. Portesi, E. Mezzetti, Local thermal bistability in MgB_2 microwave coplanar resonators: Opposite jumpwise response to weak-link switching and to vortex avalanches, Applied Physics Letters 94 (5) (2009) 052505.

[15] D. Hafner, M. Dressel, M. Scheffler, Surface-resistance measurements using superconducting stripline resonators, Review of Scientific Instruments 85 (1) (2014) 014702.

[16] B. Avenhaus, A. Porch, M. Lancaster, S. Hensen, M. Lenkens, S. Orbach-Werbig, E. Muller, U. Dahne, N. Tellmann, N. Klein, C. Dubourdieu, J. Senateur, O. Thomas, H. Karl, B. Stritzker, J. Edwards, R. Humphreys, Microwave properties of YBCO thin films, IEEE Transactions on Applied Superconductivity 5 (2) (1995) 1737–1740. doi:10.1109/77.402913.

[17] S. K. Remillard, D. Kirkendall, G. Ghigo, R. Gerbaldo, L. Gozzelino, F. Laviano, Z. Yang, N. Mendelsohn, B. Ghamsari, B. Friedman, et al., Microwave nonlinearity and photoresponse of superconducting resonators with columnar defect micro-channels, Superconductor Science and Technology 27 (9) (2014) 095006.

[18] I. B. Vendik, E. L. Kollberg, O. G. Vendik, T. B. Samoilova, High temperature superconductor devices for microwave signal processing, Skladen Company, 1997.

[19] F. Sirois, F. Grilli, A. Morandi, Comparison of constitutive laws for mod-

eling high-temperature superconductors, IEEE Transactions on Applied Superconductivity 29 (1) (2019) 1–10. doi:10.1109/TASC.2018.2848219.
[20] R. H. Koch, V. Foglietti, W. J. Gallagher, G. Koren, A. Gupta, M. P. A. Fisher, Experimental evidence for vortex-glass superconductivity in Y – Ba – Cu – O, Phys. Rev. Lett. 63 (1989) 1511–1514. doi:10.1103/PhysRevLett.63.1511.
[21] P. Lahl, R. Wordenweber, Nonlinear microwave properties of HTS thin film coplanar devices, IEEE Transactions on Applied Superconductivity 13 (2) (2003) 2917–2920. doi:10.1109/TASC.2003.812046.
[22] C. C. Chin, D. E. Oates, G. Dresselhaus, M. S. Dresselhaus, Nonlinear electrodynamics of superconducting NbN and Nb thin films at microwave frequencies, Phys. Rev. B 45 (1992) 4788–4798. doi:10.1103/PhysRevB.45.4788.
[23] L. Krusin-Elbaum, L. Civale, V. M. Vinokur, F. Holtzberg, "phase diagram" of the vortex-solid phase in y-ba-cu-o crystals: A crossover from single-vortex (1d) to collective (3d) pinning regimes, Phys. Rev. Lett. 69 (1992) 2280–2283. doi:10.1103/PhysRevLett.69.2280.
[24] J. I. Gittleman, B. Rosenblum, Radio-frequency resistance in the mixed state for subcritical currents, Physical Review Letters 16 (17) (1966) 734.
[25] M. Golosovsky, M. Tsindlekht, D. Davidov, High-frequency vortex dynamics in $YBa_2Cu_3O_7$, Superconductor Science and Technology 9 (1) (1996) 1. doi:10.1088/0953-2048/9/1/001.
[26] G. Blatter, M. V. Feigel'man, V. B. Geshkenbein, A. I. Larkin, V. M. Vinokur, Vortices in high-temperature superconductors, Rev. Mod. Phys. 66 (1994) 1125–1388. doi:10.1103/RevModPhys.66.1125.
[27] D. Bafia, M. Checchin, A. Grassellino, A. Romanenko, J. Zasadzinski, Investigating the anomalous frequency variations near t_c of nb srf cavities, Tech. rep., Fermi National Accelerator Lab.(FNAL), Batavia, IL (United States) (2022).
[28] H. Ueki, M. Zarea, J. Sauls, Electromagnetic response of superconducting rf cavities, arXiv preprint arXiv:2209.11752 (2022).
[29] K. Wohlleben, Influence of proton irradiation on the critical current density $j_c(B, T)$ of NbTi, Journal of Low Temperature Physics 13 (1973) 269–286.
[30] M. Zarea, H. Ueki, J. Sauls, Effects of anisotropy and disorder on the superconducting properties of niobium, arXiv preprint arXiv:2201.07403 (2022).
[31] M. A. Tanatar, D. Torsello, K. R. Joshi, S. Ghimire, C. J. Kopas, J. Marshall, J. Y. Mutus, G. Ghigo, M. Zarea, J. A. Sauls, R. Prozorov, Anisotropic superconductivity of niobium based on its response to nonmagnetic disorder, Phys. Rev. B 106 (2022) 224511. doi:10.1103/PhysRevB.106.224511.